

Received 7 January; accepted 4 March 2002.

1. Farrington, J., Moore, A. J., Tilbury, N., Church, J. & Biemond, P. D. in *Proc. IEEE 3rd Int. Symp. on Wearable Computers 1999* 107–113 (IEEE, San Francisco, 1999).
2. Morozumi, S. in *Liquid Crystals: Applications and Uses* (ed. Bahadur, B.) Vol. 1, 181 (World Scientific, Singapore, 1990).
3. Kamiya, H. et al. in *SID 01 Digest of Technical Papers, 2001 Int. Symp.* Vol. 32, 1354–1357 (Society for Information Display, 2001).
4. Vaz, N. A., Smith, G. W. & Montgomery, G. P. A light control film composed of liquid crystal droplets in a UV-curable polymer. *Mol. Cryst. Liq. Cryst.* **146**, 1–15 (1987).
5. Doane, J. W., Vaz, N. S., Wu, B. G. & Zumer, S. Field controlled light scattering from nematic microdroplets. *Appl. Phys. Lett.* **48**, 269–271 (1986).
6. Hirai, Y., Niyama, S., Kumaim, H. & Gunjima, T. Phase diagram and phase separation in LC/prepolymer mixture. *Proc. SPIE Int. Soc. Opt. Eng.* **1257**, 2–8 (1990).
7. Bowley, C. C., Yuan, H. & Crawford, G. P. Morphology of holographically-formed polymer dispersed liquid crystals (H-PDLC). *Mol. Cryst. Liq. Cryst. Technol. A* **331**, 2069–2076 (1999).
8. Yamada, N., Kohzaki, S., Funada, F. & Awane, K. Axially symmetric aligned microcell (ASM) mode: electro-optical characteristics or new display mode with excellent wide viewing angle. *J. Soc. Inform. Disp.* **3**, 155–158 (1995).
9. Park, E. Y., Taheri, B., West, J. L. & Palfy-Muhoray, P. in *SID 00 Digest of Technical Papers, 2000 Int. Symp.* Vol. 31, 782–785 (Society for Information Display, 2000).
10. Vorflusev, V. & Kumar, S. Phase-separated composite films for liquid crystal displays. *Science* **283**, 1903–1905 (1999).
11. Qian, T., Kim, J.-H., Kumar, S. & Taylor, P. L. Phase-separated composite films: Experiment and theory. *Phys. Rev. E* **61**, 4007–4010 (2000).
12. Broer, D. J., Lub, J. & Mol, G. N. Wide-band reflective polarizers from cholesteric polymer networks with a pitch gradient. *Nature* **378**, 467–469 (1995).
13. Kiefer, R., Weber, B., Windscheid, F. & Baur, G. in *Proc. 12th Int. Display Conf., Japan Display '92* 547–550 (1992).
14. Oh-e, M., Ohta, M., Aratani, S. & Kondo, K. in *Proc. 15th Int. Display Conf. Asia Display '95* 577–580 (1995).
15. Bobrov, Y. A. et al. Novel dichroic polarizing materials and approaches to large-area processing. *Mater. Res. Soc. Symp. Proc.* **508**, 225–228 (1998).

## Acknowledgements

We thank J. Lub for synthesis of the stilbene dimethacrylate and for discussions.

## Competing interests statement

The authors declare that they have no competing financial interests.

Correspondence and requests for materials should be addressed to D.J.B. (e-mail: dick.broer@philips.com).

# Distribution of breaking waves at the ocean surface

W. Kendall Melville & Peter Matusov

Scripps Institution of Oceanography, University of California, San Diego, La Jolla, California 92093-0213, USA

Surface waves play an important role in the exchange of mass, momentum and energy between the atmosphere and the ocean. The development of the wave field depends on wind, wave-wave and wave-current interactions and wave dissipation owing to breaking, which is accompanied by momentum fluxes from waves to currents. Wave breaking supports air-sea fluxes of heat and gas<sup>1,2</sup>, which have a profound effect on weather and climate. But wave breaking is poorly quantified and understood. Here we present measurements of wave breaking, using aerial imaging and analysis, and provide a statistical description of related sea-surface processes. We find that the distribution of the length of breaking fronts per unit area of sea surface is proportional to the cube of the wind speed and that, within the measured range of the speed of the wave fronts, the length of breaking fronts per unit area is an exponential function of the speed of the front. We also find that the fraction of the ocean surface mixed by breaking waves, which is important for air-sea

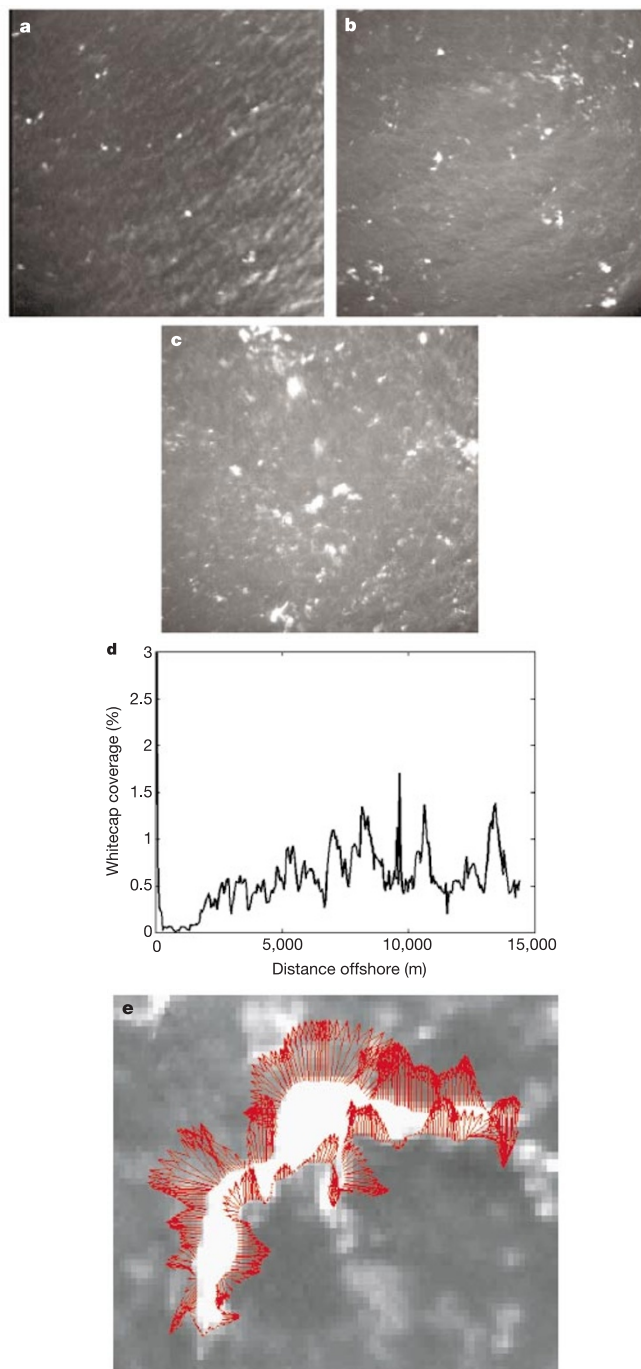


**Figure 1** Whitecap imaging and image processing. **a–c**, Cropped images showing approximately  $160 \text{ m} \times 160 \text{ m}$  of the sea surface taken from an altitude of approximately 400 m for mean wind speeds,  $U_{10}$ , of 7.2, 9.8 and  $13.6 \text{ m s}^{-1}$ , respectively, off the coast of North Carolina in the autumn of 1999. We note the increasing density of whitecaps with wind speed and their random shapes. Individual whitecaps are defined by a brightness threshold, which was varied to ensure that the results presented are not sensitive to the threshold chosen. **d**, The fractional area of the sea surface covered by whitecaps,  $A_w$ , ('whitecap coverage') as the aircraft flew offshore for a distance of approximately 15 km. We note the initial decline in  $A_w$  across the surf zone and then the increase offshore. There are large fluctuations at spatial scales of  $O(1\text{--}10 \text{ km})$  that may be due to both local wind and wave modulations. **e**, The result of processing a single whitecap using the PIV technique in which the normal velocity of the boundary of the whitecap is resolved at a scale of approximately 50 cm. The mean velocity of the whitecap was computed from the mean of the elemental velocities, and then only the elements located at the boundary within  $\pm 90^\circ$  from the mean velocity of the whitecap, having positive outward normal velocities directed outside the boundary, were included in the  $\Delta(c)$  statistics.

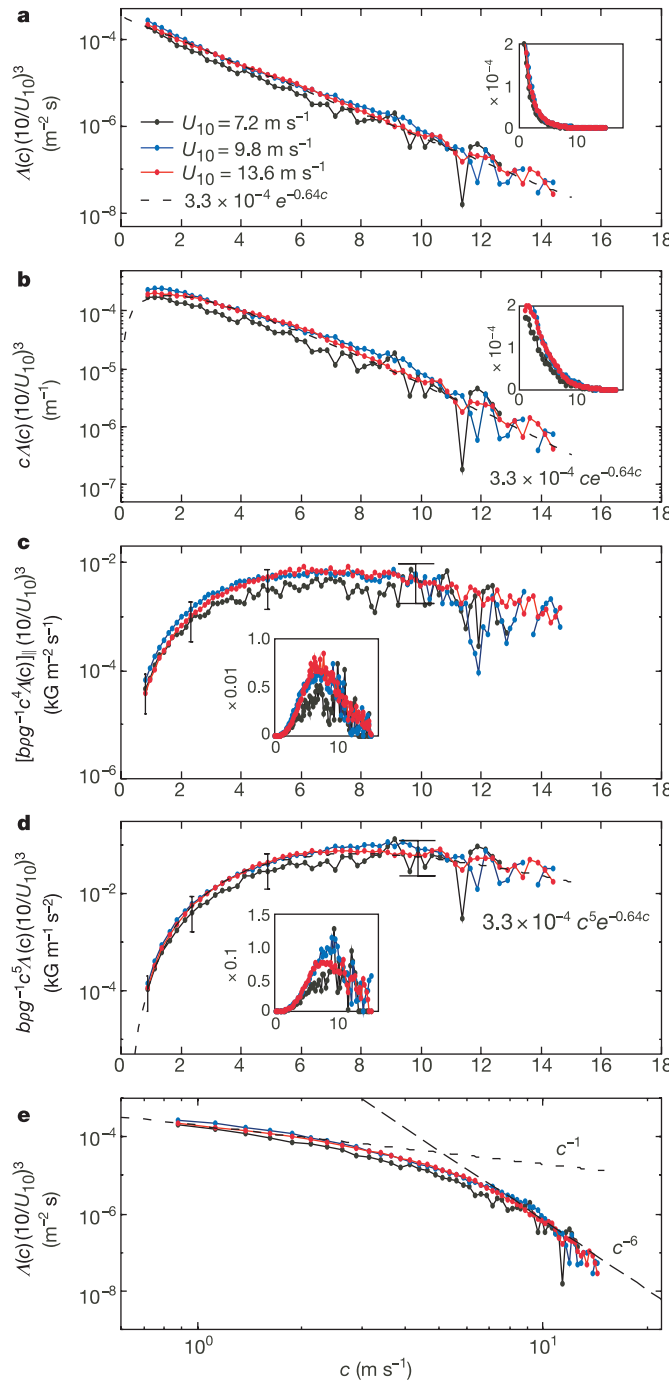


**Figure 2** Measurements of  $\Delta(c)$  and its moments. **a**, Binned measurements of  $\Delta(c)$  (from data like that in Fig. 1e, weighted by  $U_{10}^{-3}$ ) showing that to a very good approximation the average length of breaking fronts in  $(c, c + dc)$  per unit area of sea surface increases like  $U_{10}^3$  and decays exponentially with  $c$  as follows:  $\Delta(c) = 3.3 \times 10^{-4} e^{-0.64c}$ . This PIV method was checked against simpler measurements of the rate of increase of area of individual whitecaps. The line integral of the outward flux vectors around the perimeter of the whitecap is equal to the rate of increase of area of the whitecap, which can easily be determined by other methods. It was found that if the length of the breaking front was on average set to one-third of the perimeter, then  $\Delta(c)$  determined by the two methods agreed very well, especially for the smaller values of  $c$ . Linear plots of the data (insets) show that the  $U_{10}^3$  scaling is not an artefact of the log-linear plot. See also **b** and **c**. **b**, The weighted (by  $U_{10}^{-3}$ ) first moment of  $\Delta(c)$  which corresponds to the fractional area swept out (turned over) by breakers in the speed range  $(c, c + dc)$ . This and higher moments are computed from the raw data rather than just multiplying the data in **a** by  $c^n$ , although the moments based on the exponential fit to the binned values of  $\Delta(c)$  agree very well. The first moment approaches a maximum at smaller  $c$ , demonstrating the significance of the

slower/smaller scales in breaking/mixing the surface. **c**, The weighted (by  $U_{10}^{-3}$ ) fourth moment of  $\Delta(c)$ ,  $c^4 \Delta(c)_{||}$ , which corresponds to the momentum flux from waves to currents due to whitecaps, with the subscript '||' referring to the component in the wind direction. Now the momentum flux is a maximum in the intermediate range of breaking speeds. Vertical bars show the range of  $b$  from laboratory data<sup>5</sup>. **d**, The weighted (by  $U_{10}^{-3}$ ) fifth moment of  $\Delta(c)$ , which corresponds to the energy lost from the wave field owing to breaking: 'wave-dissipation'. Again, the weighted curves collapse very well at the smaller values of  $c$ , and the maximum moves to higher  $c$  for the higher moment. In **c** and **d**, we have used the numerical value of  $b$  determined in laboratory experiments on unsteady breaking<sup>5</sup> ( $8.5 \times 10^{-3}$ ) and the vertical error bars reflect the range of that parameter. The linear insets in **c** and **d** show that the integrals of these moments would converge over the range of the experiments. **e**, The same data as in **a** but now plotted as log-log, showing that  $\Delta(c)$  varies like  $c^{-1}$  and  $c^{-6}$  for the smallest and largest values of  $c$ , respectively. The  $c^{-1}$  and  $c^{-6}$  behaviour are consistent with local approximations to the exponential decay of  $\Delta(c)$ . The  $c^{-6}$  behaviour is consistent with a prediction of local equilibrium by Phillips<sup>3</sup>.

exchange, is dominated by wave breaking at low velocities and short wavelengths.

Wave breaking is a process that is vital to many aspects of air–sea interaction and remote sensing of the oceans. It limits the height of surface waves, transfers momentum flux from waves to currents and ‘renews’ the surface (a significant aspect of air–sea heat-flux and gas-flux processes). Wave breaking also generates marine aerosols—which are important in biogeochemistry, cloud physics, atmospheric radiation balances and hurricane thermodynamics—and entrains bubbles, which modify the optical properties of the ocean surface and thereby the interpretation of ocean colour. Our ability to quantify these processes has been inhibited by the absence of good quantitative measures of the distribution of breaking.

Phillips<sup>3</sup> introduced  $\Lambda(c)dc$ , the average length of breaking crests per unit area of ocean surface travelling at velocities in the range  $(c, c + dc)$ , as a statistical description of breaking, its kinematics and dynamics. The dynamical description is based in part on laboratory measurements, and in part on physical/dimensional arguments<sup>4–8</sup> that the energy dissipation per unit length of breaking crest is given by:

$$\epsilon_1 = b\rho_w g^{-1} c^5 \quad (1)$$

where  $\rho_w$  is the density of water,  $g$  gravity,  $c = |\mathbf{c}|$ , and, for unsteady breaking,  $b$  is a number in the range  $O(10^{-3}–10^{-2})$  that depends on the steepness of the waves<sup>5</sup>. Radar measurements of  $\Lambda$  suggest that  $b$  could be an order of magnitude smaller<sup>9</sup>, but the indirect nature of the measurements may account for some of the difference. Wave energy and momentum densities are related by  $M = E/c$ , with the momentum flux per unit length of crest given by  $m_1 = b\rho_w g^{-1} c^4$ . Here we use an airborne video system, along with a motion package and differential global positioning system (GPS), to obtain image sequences of breaking waves in an Earth frame.

Measurements were made from light aircraft flights at approximately  $50 \text{ m s}^{-1}$  airspeed and 450 m altitude off North Carolina, USA, in 1999 during the shoaling waves experiment (SHOWEX); extending up to 60 km offshore over water of 20–50 m depth. The same ground tracks were flown at altitudes of 15–25 m for wind and wave measurements.

Figure 1a–c shows examples of cropped ( $256 \times 256$  pixels;  $160 \times 160 \text{ m}$ ) images of whitecaps at approximately 0.6-m resolution for the three wind speeds. The increasing fractional area of whitecap coverage,  $A_w$ , with wind speed<sup>10,11</sup> is apparent in Fig. 1. The variability of  $A_w$  over scales of the order of a kilometre (Fig. 1d) is remarkable, suggesting that the incidence of breaking may ultimately be related to very local conditions. This variability could come from the local wind, or modulation of the surface wave field itself<sup>12</sup>.

Individual whitecaps were tracked and measured for 5–10 s. During that time, their areas could be increasing, at a maximum, or decreasing. Active breaking corresponds to expanding whitecaps. Whitecap decay corresponds to a decrease in size as entrained bubbles rise to the surface<sup>13,14</sup> and burst to form aerosols. Without detailed measurements of the evolution of the whitecap (see below), it was impossible to associate a unique velocity of advance,  $c$ , with each whitecap during its growth. However, by using particle imaging velocimetry (PIV)<sup>15</sup>, we could measure the velocity of the local boundary of the whitecap, thereby giving  $\Lambda(c)dc$  (see Methods). Figure 1e shows the results for a single large whitecap. Thus  $\Lambda(c)dc$  is accumulated from the individual elements of the boundary rather than attributing single values of  $\Lambda_i$  and  $c_i$ , say, to each whitecap (see Methods). Data were collected at three averaged ten-metre wind speeds,  $U_{10} = 7.2, 9.8$  and  $13.6 \text{ m s}^{-1}$ , in a series of flights.

Figure 2a shows that when weighted by  $U_{10}^{-3}$  (ref. 3), the measurements of  $\Lambda(c)$  collapse approximately onto a single exponential curve,  $\Lambda(c) = 3.3 \times 10^{-4} e^{-0.64c}$ , over the measured range of  $c$ . The surface wave field, and hence the breaking statistics, depend on fetch, the distance the wind has blown over the ocean surface,

and other factors, so the apparent dependence on only wind speed here is probably due to the fetch being approximately the same for each measured wind event at this location.

For small values of  $c$ ,  $\Lambda(c)$  varies like  $c^{-1}$  and for larger  $c$  values like  $c^{-n}$ , where  $n > 1$ . (In general, if  $\Lambda(c) = ae^{-bc}$ , where  $a$  and  $b$  are constants, it osculates with the curve  $y = dc^{-n}$  ( $d = \text{constant}$ ,  $n \geq 1$ ), at  $c = n/b$  when  $d = ae^{-n(n/b)^a}$ .)  $\Lambda(c) \propto c^{-6}$  provides a good approximation for larger  $c$  values, consistent with Phillips<sup>3</sup> equilibrium subrange (see Fig. 2b). A smaller slope at smaller  $c$  is

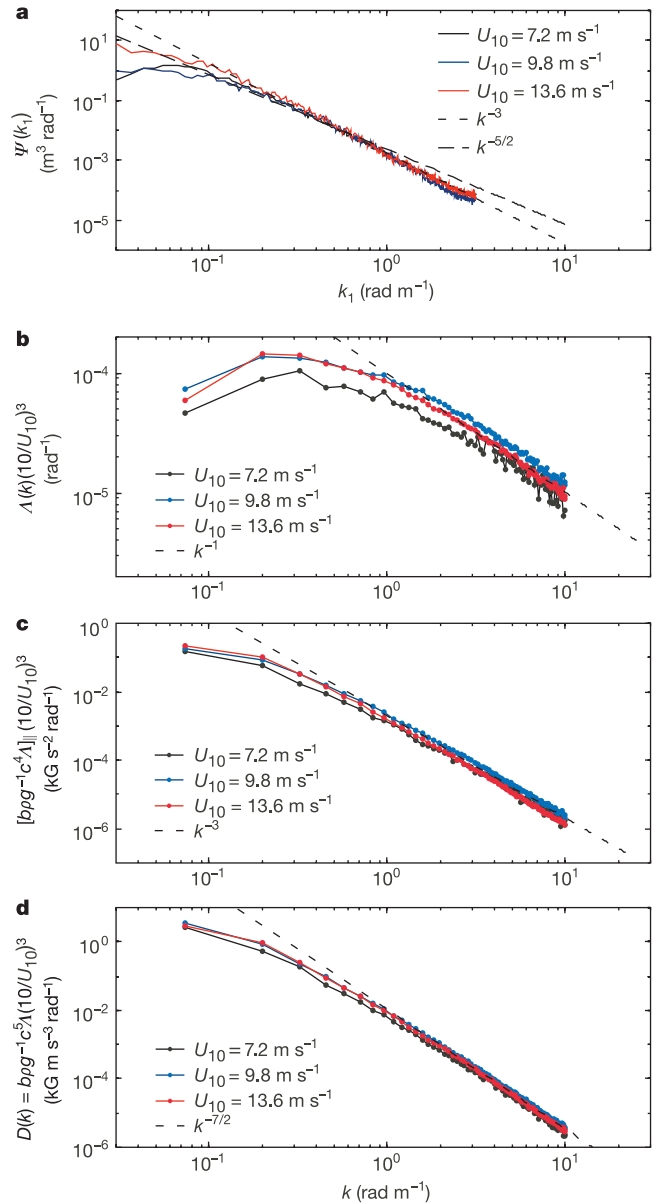


**Figure 3** Wavenumber spectra of the surface waves and of  $\Delta(c)$  and its moments. **a**, One-dimensional wavenumber spectra of the sea surface displacement measured using laser altimeters on the aircraft in averaged pairs of upwind and downwind flights (one-dimensional samples of the surface) separated briefly in time. Owing to low-wavenumber noise, the data are not considered accurate for wavenumbers below approximately  $0.1 \text{ rad m}^{-1}$ . Note that wavenumbers  $O(0.1) \text{ rad m}^{-1}$  and higher transition from a  $k^{-5/2}$  slope to a  $k^{-3}$  slope at all wind speeds, consistent with  $k^{-5/2}$  and  $k^{-3}$  omnidirectional spectra, respectively. **b**, Weighted distribution of  $\Delta(k)$  determined from the data of Fig. 2 using  $k/\tanh(kh) = g/c_p^2 = (0.8)^2 g/c^2$  to transform from  $c$  to  $k$ ;  $h = 22.5 \pm 2.5 \text{ m}$ . For large  $k$  the curves decay like  $k^{-1}$ . **c**, The downwind component of the weighted momentum flux from breaking waves as a function of wavenumber (compare Fig. 2c). For high wavenumbers the decay is like  $k^{-3}$ . **d**, The weighted wave dissipation due to breaking as a function of wavenumber. For high wavenumbers the decay is like  $k^{-7/2}$ .

qualitatively consistent with the recent equilibrium model of Hara and Belcher<sup>16</sup> (a refinement of Phillips' model), but important quantitative differences remain (see below).

Figure 2c shows the first moment of  $\Lambda(c)$  (based on the raw data), where  $c\Lambda(c)dc$  is the fraction of the surface area swept out per unit time by breaking waves in the speed range  $(c, c + dc)$ , and the probability per unit time of breaking at a point on the ocean surface. Given the exponential form for  $\Lambda(c)$ , we expect a maximum in the  $n$ th moment in the neighbourhood of  $c = (n/0.64) \text{ m s}^{-1}$ . For the first moment this is  $1.6 \text{ m s}^{-1}$ , close to the lower limit of our measurements.

Using  $b = 8.5 \times 10^{-3}$  (ref. 5), Fig. 2d and e shows the weighted (by  $U_{10}^3$ ) fourth and fifth moments of  $\Lambda(c)$ , corresponding to the momentum flux from the waves to currents through breaking, and the energy lost by the wave field, respectively. The cubic wind-speed dependence collapses the data for smaller values of  $c$ , whereas some statistical scatter due to fewer events remains at larger  $c$ . Also shown are insets of the moments, demonstrating that even on a linear scale the  $U_{10}^3$  scaling is robust, especially at the larger wind speeds. Within the scatter at the larger values of  $c$ , the integrals of the momentum flux and dissipation distributions converge. The maxima in these moments, inferred from the distribution for  $\Lambda(c)$ , would be at  $6.4$  and  $8 \text{ m s}^{-1}$ , respectively, consistent with the data.

Wave models are usually represented in the wavenumber domain,  $k$ . This raises the issue of mapping from  $c$  to  $k$ . Because breaking is local in space, its spectral representation in the wavenumber plane must be broad-banded. However, measurements suggest that most of the dissipation is around the frequency of the characteristic breaking wave, and that  $c$  is approximately 80% of the characteristic

linear phase speed of the wave (see also ref. 9). Thus  $k = g/c_p^2 = (0.8)^2 g/c^2$ , where  $c_p^2 = gk^{-1} \tanh(kh)$  is the phase speed of the waves,  $h$  the water depth, and  $\Lambda(k)$  and its moments can then be represented, as shown in Fig. 3, along with the one-dimensional wavenumber spectra of the surface waves. Below  $k_1 = 0.1 \text{ rad m}^{-1}$  the surface wavenumber spectra are prone to errors, but display power-law behaviour at larger values of  $k_1$ . For  $k_1 = (0.1, 1) \text{ rad m}^{-1}$ , the spectra are approximately proportional to  $k_1^{-5/2}$ , consistent with the Phillips<sup>3</sup> prediction of a  $k^{-7/2}$  two-dimensional spectrum. For  $k_1 > 1 \text{ rad m}^{-1}$ , the  $k_1^{-3}$  one-dimensional wavenumber spectrum corresponds to a two-dimensional  $k^{-4}$  spectrum, and a  $k^{-3}$  omni-directional spectrum<sup>17</sup>. The spectra of  $\Lambda(k)$  and the fourth and fifth moments decay like  $k^{-1}$ ,  $k^{-3}$  and  $k^{-7/2}$ , respectively, for  $k > 1 \text{ rad m}^{-1}$ .

The directional properties of  $\Lambda(c)$ , the momentum flux and the energy dissipation are shown for the three different mean wind vectors in Fig. 4. Some elements of the whitecap boundaries are travelling slowly upwind, but when the higher moments are taken, the momentum flux and dissipation are clearly associated with waves breaking approximately symmetrically about the mean downwind direction. In weaker winds the symmetry is not so strong. The symmetry of the momentum flux distribution implies that the net momentum flux is approximately in the wind direction.

The existence of an approximate equilibrium subrange<sup>3</sup> in the spectrum of the surface wave field would be of considerable importance for describing the surface wave field and related air-sea fluxes. These measurements offer some insight into this question. Our measurements of  $\Lambda(c) \propto c^{-6}$ , and  $\psi(k_1) \propto k_1^{-5/2}$ , are quantitatively consistent with the equilibrium theory of Phillips<sup>3</sup> for a subrange of

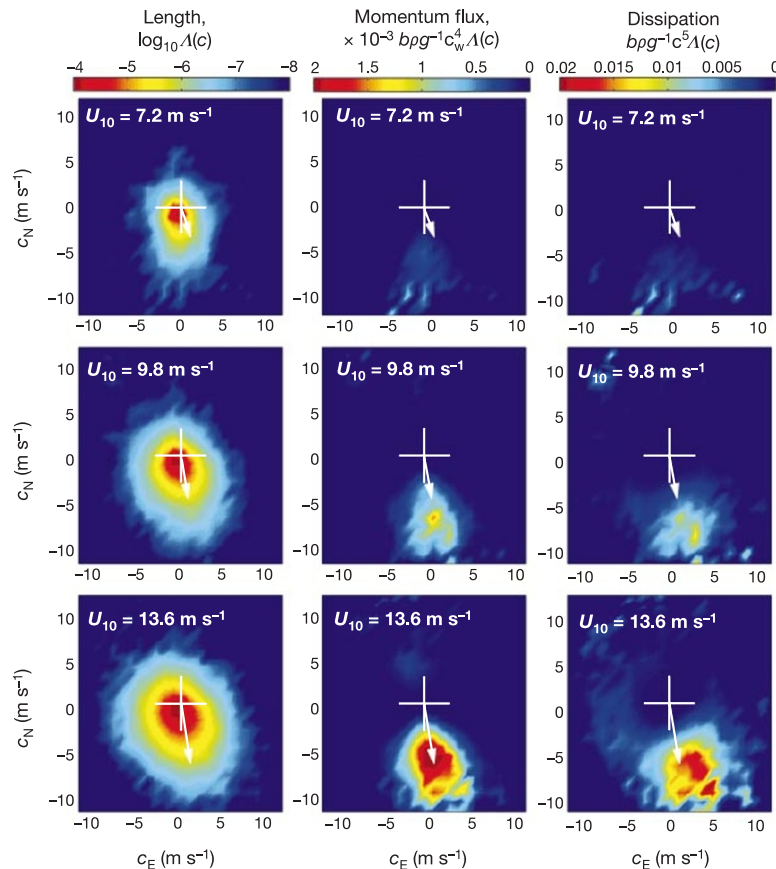


**Figure 4** Directional distributions of  $\Lambda(c)$  and its moments. **a**, Distributions with respect to the northerly and easterly components of  $c(c_N, c_E)$  of  $\Lambda(c)$  along with the average wind direction (arrow). The dominant orientation is close to the wind direction. However, there is some upwind and cross-wind breaking (this is accentuated by the logarithmic colour scale of the amplitude). The extremes of these distributions account for the few outliers at

speeds greater than the mean wind speeds in Fig. 2a, e. **b**, The corresponding momentum flux from waves to currents due to breaking for the three wind speeds. As the wind increases the region of significant momentum flux becomes approximately symmetrical about the downwind direction (compare Fig. 2b). **c**, The corresponding distribution of the dissipation with  $(c_N, c_E)$ .



larger  $c$  and smaller  $k$  values, respectively. However, the  $c^{-6}$  behaviour is only a local approximation to the exponential distribution.

Hara and Belcher<sup>16</sup> predict an equilibrium range bounded by two asymptotic regimes separated by a 'sheltering wavenumber',  $k_s$ . For  $k \ll k_s$ , they support Phillips' predictions. At larger wavenumbers,  $k > k_s$ , sheltering by the longer waves produces less growth as momentum flux is lost to the longer waves. The significant decrease in the dissipation that we find for smaller  $c$  and larger  $k$  are qualitatively consistent with their model, as are the measured one-dimensional surface wavenumber spectra (see also Banner *et al.*<sup>18</sup>); however, important differences remain since we find the omni-directional dissipation  $D(k)$  decaying as  $k^{-7/2}$  compared to their prediction of  $k^{-5/2}$ . Furthermore, their predictions of  $k_s$  for our range of wind speeds are all greater than  $100 \text{ rad m}^{-1}$ , well outside the range of our data and above their estimate of the high wavenumber cut-off for surface waves<sup>19,20</sup>.

In estimating the dissipation from the measurements of  $\Lambda(c)$ , we have assumed that the numerical parameter,  $b$ , is effectively constant; this is consistent with ref. 3, and our measurements of  $\Lambda(c)$  over a limited range of  $c$ . However, laboratory measurements<sup>5</sup> show that  $b$  increases approximately linearly with wave slope, or with breaking going from spilling to plunging. A decrease in  $b$  with increasing  $c$  would lead to a small decrease in the dissipation.

The exponential distribution of  $\Lambda(c)$  is consistent with the fact that  $\Lambda$  must remain bounded for small  $c$ , because there cannot be an infinite length of orthogonally finite structures in a finite area. Hence,  $c\Lambda(c) \rightarrow 0$  as  $c \rightarrow 0$ , and there must be a maximum in  $c\Lambda(c)$  for small  $c$ ; although the data do not clearly represent it. The e-folding scale, found here to be constant, is expected to be a function of the fetch. With the shift in the peak of the wave spectrum to lower frequencies (higher  $c$ ) as the fetch increases, we expect  $\Lambda(c)$ , and hence the e-folding scale, to increase; that is, there will be more breaking at larger  $c$ .

These measurements are limited to whitecaps with significant air entrainment. Breaking gravity-capillary waves near the minimum phase speed ( $23 \text{ cm s}^{-1}$ ), which are not measured by these techniques, may display different behaviour. Thermal imagery, rather than visible imagery, is likely to be important for resolving the statistics of microscale (gravity-capillary) breaking<sup>2</sup>.

This work has demonstrated that breaking, a process vital to many aspects of air-sea interaction, can be measured by remote techniques, and that  $\Lambda(c)$  and its moments, which are directly relevant for ocean-surface processes, can be simply characterized. We find that the momentum flux to currents, and wave dissipation, are proportional to  $U_{10}^3$  and dominated by intermediate scale waves. The fraction of the ocean surface mixed ('renewed') by breaking waves per unit time  $c\Lambda(c)$ , an important component of air-sea heat and gas flux models, is proportional to  $U_{10}^3$  and is dominated by the slower (shorter) breaking waves. Marine spray/aerosol generation is poorly understood with model predictions varying by orders of magnitude<sup>21</sup>. However, the direct generation of spray by breaking fronts is simply proportional to  $\Lambda(c)$ , albeit with additional dependences on  $c$  and the Weber number. Finally, recent research demonstrates that the optical properties of ocean surface waters are influenced by bubbles entrained by breaking waves<sup>22</sup>, so that accurate optical remote sensing of ocean productivity (such as with chlorophyll  $a$ ) must account for the statistics of breaking as described here.  $\square$

## Methods

The video camera (Pulnix TM-9700,  $484 \times 768$  pixels), attached to a six-degrees-of-freedom motion package (Watson BA-604), was suspended in a pod beneath the Long EZ aircraft. Images were acquired and stored at 5 Hz. The data/image acquisition computer and GPS receiver and antenna were housed under the aircraft's canopy. A base station provided differential-GPS location of the aircraft at 10 Hz. The aircraft's nominal altitude for image-acquisition flights was 450 m, giving pixel sizes of approximately 50 cm.

On the basis of the brightness distribution of each image, a threshold was chosen to distinguish breaking waves and their boundaries from the background. A range of

thresholds was tested to ensure insensitivity of the results to the specific choice. Only actively breaking (expanding) whitecaps were considered. Square sub-images ( $5 \times 5$  pixels on a side) were used for particle imaging velocimetry (PIV) analysis<sup>15</sup> of the velocity of the whitecap boundary. With a  $5 \times 5$  window the velocity of the boundary was calculated over a 2.5-m segment, approximately every 0.5 m along the boundary: a running average. PIV processing resolves the peak in the correlation to within half a pixel, or 0.3 m normal to the boundary.

In interpreting the whitecap motion, we need to avoid two effects: Doppler shifting (advection); and straining, due to longer waves and swell. In the laboratory<sup>6,7</sup>, the upstream boundary of the whitecap remains effectively stationary in the absence of the orbital motion of the following waves, while the breaking front moves forward at approximately 80% of the phase speed. In the ocean the advection of the whitecap by longer waves cannot be neglected and so we choose to remove this effect by defining the speed of advance of the whitecap relative to the upstream, or rearward, edge of the whitecap. To avoid these effects we process the data in the following way: (1) a mean velocity is calculated for each whitecap from all the velocities of the boundary elements; (2) the rear of the whitecap is defined as the points on the contour located within an angle of  $\pm 60^\circ$  from the centroid of the whitecap in the direction opposite to that of the mean whitecap velocity; (3) the mean velocity of the rear of the whitecap is subtracted from all velocity vectors in the whitecap profile; (4) the components of velocity normal to the whitecap boundary are calculated; (5) the front of the whitecap is defined as the points on the contour located within an angle of  $\pm 90^\circ$  from the centroid in the direction of the mean velocity of the whitecap; (6) the statistical analysis includes only elements of the contour belonging to the front of the whitecap; and (7) all elements of the processing were tested for sensitivity to specific choices of thresholds.

To summarize,  $\Lambda(c)dc = (1/A_s)\sum_{\substack{c_{\perp i} \in [c, c+dc] \\ A_i}} A_i dc$ , where  $A_i$  are lengths of the whitecap boundary elements which lie within  $\pm 90^\circ$  of the whitecap mean velocity relative to the centroid (calculated for each whitecap), and  $c_{\perp i}$  is the outward velocity component normal to  $A_i$ . The summation is performed for all whitecap data within the imaged (swept) area  $A_s$ .

The significance of the straining of the whitecap by the orbital motion of the longer waves can be estimated by accounting for the relative motion between the forward and rearward faces of the whitecap. If the speed of advance of the whitecap scales with the phase speed of the breaking wave,  $c_b$ , and if the length of the whitecap is at most the wavelength of the breaking wave, the relative error in  $c$  is  $O(a_1 k_1) c_b / c_1$ , where  $a_1 k_1$  is the slope of the longer wave and  $c_1$  its phase speed. If both  $a_1 k_1$  and  $c_b / c_1$  are much less than unity, the error will be very small. As  $c_b / c_1$  tends to unity, the 'long' wave becomes the breaking wave and the laboratory data<sup>6</sup> show that the issue of straining becomes moot.

One-dimensional wavenumber spectra of surface waves were measured using surface displacement measurements by three Riegl laser altimeters (corrected by a GPS-based aircraft motion/altitude system) during the upwind and downwind low altitude flight legs along the same track as the image data were acquired. In computing the wave spectra the following assumptions have been made: (1) the wind waves are predominantly propagating in the direction of the wind; (2) the statistical properties of the surface are stationary; and (3) the flight track was almost straight with transverse aircraft speeds small compared to the along-track component.

We can show that, using the speed over the ground to transform the time series of sea surface elevation to spatial series and averaging, the (perceived) upwind and downwind wavenumber spectra lead to errors in the wavenumber of  $O(cU_a/V_a^2)$ , where  $c$  is the phase speed of the waves,  $U_a$  the wind speed at the aircraft elevation, and  $V_a$  the aircraft speed. For these experiments this error is in the range of 0.3–6%.

Using the aircraft position/speed data, the surface elevation data were interpolated to a regular sampling interval in space. Spectra were calculated within a running 1,024-point window ( $\sim 20$  s,  $\sim 1$  km), and averaged over the track length of  $\sim 20$  km.

All data presented here were collected during weather events with winds directed nearly parallel to the shoreline (within  $5\text{--}10^\circ$ ). The wind-wave fetch was in the range 100–150 km. The data included in the analysis were taken no closer than 30 km to shore.

Phillips<sup>3</sup> predicted that  $\Lambda(c) \propto u_*^2 c^{-6}$ , where  $u_*$  is the friction velocity in the air. Here we scale  $\Lambda$  with  $U_{10}^3$ , since over the range of conditions of these experiments we expect the drag coefficient  $C_d \equiv (u_* / U_{10})^2$  to be constant to within a factor of  $O(1)$ .

If the waves are sufficiently long and steep, dissipation in the bottom boundary layer may need to be considered in interpreting data at large values of  $c$ . Estimates of bottom friction are site-specific and based on semi-empirical unsteady boundary-layer theory. Using recognized methods<sup>23,24</sup> and a range of bottom velocities, we find that the characteristic time for wave decay due to bottom friction in 20–25 m depth is typically  $O(10^4)$  seconds, compared to  $O(10^3)$  seconds, owing to breaking. Thus the contribution of bottom dissipation to the energy budget is small compared to dissipation due to breaking. Furthermore, measurements of  $\Lambda(c)$  in 40–50 m depth were almost indistinguishable from those in 20–25 m.

Received 28 August 2001; accepted 20 February 2002.

- Melville, W. K. The role of surface wave breaking in air-sea interaction. *Annu. Rev. Fluid Mech.* **28**, 279–321 (1996).
- Jessup, A. T., Zappa, C. J., Loewen, M. R. & Healy, V. Infrared remote sensing of breaking waves. *Nature* **385**, 52–55 (1997).
- Phillips, O. M. Spectral and statistical properties of the equilibrium range in wind-generated gravity waves. *J. Fluid Mech.* **156**, 505–531 (1985).
- Duncan, J. H. An experimental investigation of breaking waves produced by a towed hydrofoil. *Proc. R. Soc. Lond. A* **377**, 331–348 (1981).
- Melville, W. K. Energy dissipation by breaking waves. *J. Phys. Oceanogr.* **24**, 2041–2049 (1994).
- Rapp, R. J. & Melville, W. K. Laboratory measurements of deep-water breaking waves. *Phil. Trans. R. Soc. Lond. A* **331**, 735–800 (1990).
- Melville, W. K. & Rapp, R. J. Momentum flux in breaking waves. *Nature* **317**, 514–516 (1985).

8. Loewen, M. A. & Melville, W. K. Microwave backscatter and acoustic radiation from breaking waves. *J. Fluid Mech.* **224**, 601–623 (1991).
9. Phillips, O. M., Posner, F. L. & Hansen, J. P. High range resolution radar measurements of the speed distribution of breaking events in wind-generated ocean waves: Surface impulse and wave energy dissipation rates. *J. Phys. Oceanogr.* **31**, 450–460 (2001).
10. Monahan, E. C. & Muirchearthaigh, I. Optimal power-law description of oceanic whitecap coverage dependence on wind speed. *J. Phys. Oceanogr.* **10**, 2094–2099 (1980).
11. Wu, J. Variations of whitecap coverage with wind stress and water temperature. *J. Phys. Oceanogr.* **18**, 1448–1453 (1988).
12. Donelan, M. A., Longuet-Higgins, M. S. & Turner, S. Periodicity in whitecaps. *Nature* **239**, 449–451 (1972).
13. Lamarre, E. & Melville, W. K. Air entrainment and dissipation in breaking waves. *Nature* **351**, 469–471 (1991).
14. Lamarre, E. & Melville, W. K. Void-fraction measurements and sound speed fields in bubble plumes generated by breaking waves. *J. Acoust. Soc. Am.* **95**, 1317–1328 (1994).
15. Willert, C. & Gharib, M. Digital particle image velocimetry. *Exp. Fluids* **10**, 181–193 (1991).
16. Hara, T. & Belcher, S. E. Wind forcing in the equilibrium range of wind-wave spectra. *J. Fluid Mech.* (submitted).
17. Phillips, O. M. *The Dynamics of the Upper Ocean* (Cambridge Univ. Press, Cambridge, 1977).
18. Banner, M. L., Jones, I. S. F. & Trinder, J. C. Wavenumber spectra of short gravity waves. *J. Fluid Mech.* **198**, 321–344 (1989).
19. Jähne, B. K. & Riemer, K. S. Two-dimensional wavenumber spectra of smallscale water surface waves. *J. Geophys. Res.* **95**, 11531–11546 (1990).
20. Fedorov, A. V., Melville, W. K. & Rozenberg, A. An experimental and numerical study of parasitic capillary waves. *Phys. Fluids* **10**, 1315–1323 (1998).
21. Andreas, E. L. A new sea spray generation function for wind speeds up to  $32 \text{ m s}^{-1}$ . *J. Phys. Oceanogr.* **28**, 2175–2184 (1998).
22. Terrill, E. J., Melville, W. K. & Stramski, D. Bubble entrainment by breaking waves and their influence on optical scattering in the upper ocean. *J. Geophys. Res.* **106** (C8), 16815–16824 (2001).
23. Madsen, O. S., Poon, Y.-K. & Graber, H. C. in *Coastal Engineering 1988, Proc. 21st Int. Conf. Coastal Eng.* (ed. Edge, W. L.) 492–504 (American Society of Civil Engineers, New York, 1989).
24. Ardhuin, F., Herbers, T. H. C. & O'Reilly, W. C. A hybrid Eulerian-Lagrangian model for spectral wave evolution with application to bottom friction on the continental shelf. *J. Phys. Oceanogr.* **31**, 1498–1516 (2001).

#### Acknowledgements

These measurements would not have been possible without the fearless flying of T. Crawford and the support of his group at NOAA who made additional airborne measurements. We are grateful to D. Shear for his work on the initial design, construction and testing of the aerial imaging system. W.K.M. thanks T. Hara and O. Phillips for stimulating conversations on the measurement and modelling of equilibrium wave spectra, and O. Madsen and T. Herbers for advice on wave dissipation in bottom boundary layers. We are grateful to F. Veron for carefully reading and commenting on the manuscript. W.K.M. acknowledges the hospitality of the Isaac Newton Institute, Cambridge University, during the revision of this paper. This work was supported by grants from the ONR (Physical Oceanography) and the NSF (Ocean Sciences).

Correspondence and requests for materials should be addressed to W.K.M. (e-mail: kmelville@ucsd.edu).

## A new phylum of Archaea represented by a nanosized hyperthermophilic symbiont

Harald Huber\*, Michael J. Hohn\*, Reinhard Rachel\*, Tanja Fuchs\*†, Verena C. Wimmer‡ & Karl O. Stetter\*

\* Lehrstuhl für Mikrobiologie und Archaeenzentrum, Universität Regensburg, Universitätsstrasse 31, D-93053 Regensburg, Germany

‡ Max Planck Institute for Medical Research, Department of Cell Physiology, Jahnstrasse 29, 69120 Heidelberg, Germany

According to small subunit ribosomal RNA (ss rRNA) sequence comparisons all known Archaea belong to the phyla Crenarchaeota, Euryarchaeota, and—indicated only by environmental DNA sequences—to the 'Korarchaeota'<sup>1,2</sup>. Here we report the cultivation of a new nanosized hyperthermophilic archaeon from

a submarine hot vent. This archaeon cannot be attached to one of these groups and therefore must represent an unknown phylum which we name 'Nanoarchaeota' and species, which we name 'Nanoarchaeum equitans'. Cells of 'N. equitans' are spherical, and only about 400 nm in diameter. They grow attached to the surface of a specific archaeal host, a new member of the genus *Ignicoccus*<sup>3</sup>. The distribution of the 'Nanoarchaeota' is so far unknown. Owing to their unusual ss rRNA sequence, members

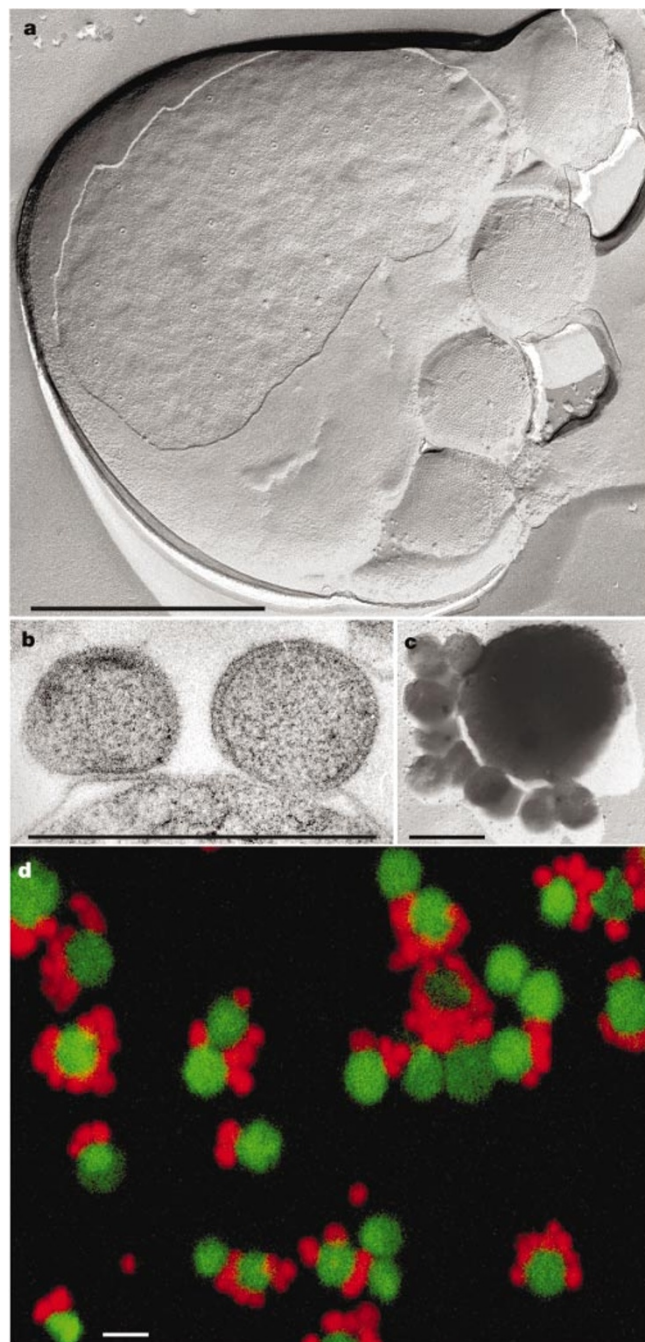


**Figure 1** Electron microscopy and fluorescence light microscopy of the 'Nanoarchaeum equitans'–*Ignicoccus* sp. coculture. **a**, Freeze-etched cell of *Ignicoccus* and four attached cells of 'Nanoarchaeum', showing their crystalline S-layer with sixfold symmetry. **b**, Ultrathin section of two cells of 'Nanoarchaeum' attached to the outer membrane of *Ignicoccus*. **c**, Cell of *Ignicoccus*, with several cells of 'Nanoarchaeum' attached on the left side; platinum-shadowed. **d**, Confocal laser scanning micrograph after hybridization with the CY3-labelled probe 515mcR ('Nanoarchaeum') and rhodamine-green-labelled probe CREN499R (*Ignicoccus*). **a–d**, Scale bar, 1.0  $\mu\text{m}$ .

† Present address: AstraZeneca GmbH, Tinsdaler Weg 183, D-22876 Wedel, Germany.